Agricultural and Forest Meteorology 203 (2015) 217–228

Agricultural and Forest Meteorology

journal homepage: www.elsevier.com/locate/agrformet

A climate generator for agricultural planning in southeastern South America

Arthur M. Greene [a,*], Lisa Goddard [a], Paula L.M. Gonzalez [a], Amor V.M. Ines [a], James Chryssanthacopoulos [b]

[a] International Research Institute for Climate and Society, Columbia University, Palisades, NY 10964, USA
[b] Center for Climate Systems Research, Columbia University, New York, NY, USA

ARTICLE INFO

Article history:
Received 28 April 2014
Received in revised form
23 December 2014
Accepted 6 January 2015
Available online 31 January 2015

Keywords:
Climate simulation
Agricultural planning
Southeastern South America
Stochastic modeling

ABSTRACT

A method is described for the generation of climate scenarios in a form suitable for driving agricultural models. The scenarios are tailored to the region in southeastern South America bounded by 25–40° S, 45–65° W, denoted here as SESA. SESA has been characterized by increasing summer precipitation, particularly during the late 20th century, which, in the context of favorable market conditions, has enabled increases in agricultural production. Since about year 2000, however, the upward tendency appears to have slowed or possibly stopped, raising questions about future climate inputs to regional agricultural yields.

The method is not predictive in the deterministic sense, but rather attempts to characterize uncertainty in near-term future climate, taking into account both forced trends and unforced, natural climate fluctuations. It differs from typical downscaling methods in that GCM information is utilized only at the regional scale, subregional variability being modeled based on the observational record. Output, generated on the monthly time scale, is disaggregated to daily values with a weather generator and used to drive soybean yields in the crop model DSSAT-CSM, for which preliminary results are discussed. The simulations produced permit assessment of the interplay between long-range trends and near-term climate variability in terms of agricultural production.

1. Introduction

During the 20th century, particularly its latter half, southeastern South America (SESA) experienced an upward trend in summer rainfall (Gonzalez et al., 2013; Liebmann et al., 2004). Together with favorable market conditions, and in the context of technological advances, this upward tendency has enabled increases in agricultural yields (Magrin et al., 2005; Viglizzo and Frank, 2006). Since about year 2000, however, the upward tendency in rainfall has slowed, or possibly reversed. Neither the steady upward trend nor its recent slowing is well-simulated by global climate models (Gonzalez et al., 2014), leaving its cause and future evolution in question. The recent decadal hindcast experiments conducted as part of the Coupled Model Intercomparison Project, phase 5 (CMIP5) do not indicate significant decadal prediction skill for SESA for either temperature or precipitation, based on initializing the models with the observed ocean state (Goddard et al., 2013). This leaves an unfilled need for useful climate information for the next few decades, in particular for the purposes of assessing the climatic contribution to potential fluctuations in agricultural yields.

We present here a methodology, not for predicting the future of SESA hydroclimate in a deterministic sense, but rather, for the characterization of future regional climate uncertainty over the next few decades. The method represents an extension of that described in earlier work in the Western Cape Province of South Africa (Greene et al., 2012, hereinafter referred to as G12), and accounts for uncertainties in both the response to anthropogenic forcing and in natural, unforced climate variability. A key question in the forcing of SESA hydroclimate concerns the influence of stratospheric ozone (e.g., Gonzalez et al., 2014); a simple method for representing the associated uncertainty is implemented. Possible cross-scale interaction is incorporated into the simulation framework as necessary. The final output is downscaled using a modification of the k-nearest-neighbor (k-NN) resampling method, applied to observational data that may have either monthly or daily time resolution. The core statistical model represents spatial covariability as well as serial autocorrelation in individual variables.

* Corresponding author. Tel.: +1 8456804436.
E-mail address: amg@iri.columbia.edu (A.M. Greene).

http://dx.doi.org/10.1016/j.agrformet.2015.01.008

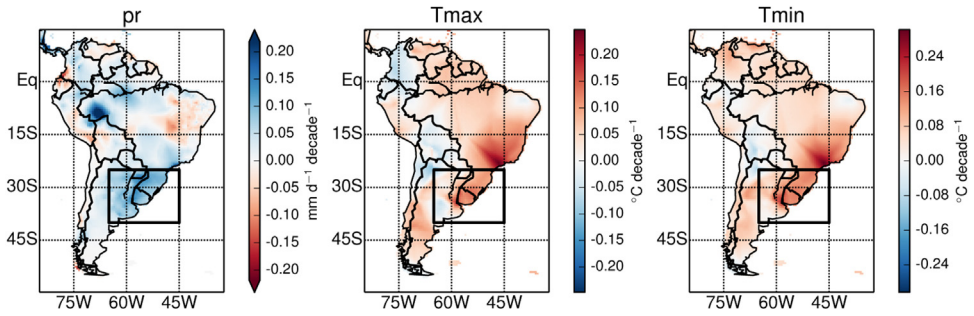

Fig. 1. Trends for precipitation and maximum and minimum daily temperatures for 1901–2011, aggregated to the seasonal (SONDJF) level. Note the reversal of colors between the precipitation and temperature scales.

The data utilized are described in Section 2 and the method in Section 3. Validation of various climate diagnostics is covered in Section 4. The downscaling component is described in Section 5 and preliminary application using an agricultural model in Section 6. A discussion and conclusions are presented in Sections 7 and 8, respectively.

2. Data

We employ both observational data and climate model simulations. When downscaling directly to the daily time step, a hybrid product based on in situ observations, satellite data and reanalysis is employed. These data types are described in turn.

2.1. Observations

The basic observational dataset employed is the TS3.21 product of the Climatic Research Unit, University of East Anglia (Harris et al., 2013), which is gridded at 0.5° and has monthly time resolution. The dataset is complete, but includes values that may have been filled, either by interpolation from nearby stations or with climatological values. The northerly extent of the study domain was limited by the presence of filled values between 20° S and 25° S. The TS3.21 data extend from 1901 through the end of 2012; since we model here a growing season (SONDJF) that crosses the year boundary, we limit the nominal range to 1901–2011, permitting the use of 111 full six-month seasons in modeling and resampling.

The study domain appears as a box in each panel of Fig. 1, which shows 1901–2011 linear trend coefficients for SONDJF for the three variables modeled: precipitation and maximum and minimum daily temperatures (Tmax and Tmin, respectively). The increasing tendency of precipitation in the SESA box can clearly be seen, as can the general increase in both of the temperature variables. The Tmax plot shows an area in the southwest of the SESA box with weakly negative coefficients, even as the rest of the box has warmed. Post-1971, however, a period of increasing global temperatures, Tmax has increased more uniformly within the box. It is of interest that Tmin increases more rapidly with time, even for trends beginning in 1901, implying a decrease in the diurnal temperature range. Future trends are modeled separately for the two temperature variables.

For precipitation, comparison was made with version 6 of the Global Precipitation Climatology Center (GPCC Schneider et al., 2011). The regional SONDJF means (3.41 mm d^{-1} and 3.58 mm d^{-1}) and standard deviations (1.34 mm d^{-1} and 1.47 mm d^{-1} for CRU and GPCC, respectively) agree fairly well, as do the regional mean 20th-century trends (0.085 and 0.086 mm d^{-1} $decade^{-1}$, respectively). Trend patterns within the SESA are also reasonably well-correlated ($r = 0.67$). Since the CRU dataset comprises similarly computed and gridded values for Tmax and Tmin, and since these variables are modeled jointly with precipitation, it was decided to utilize CRU for the work presented herein.

2.2. Climate model simulations

In G12, future regional precipitation trajectories were selected by quantile from a distribution over a set of CMIP5 climate models. For reasons to be discussed we do not utilize this procedure here. However a CMIP5 ensemble is utilized to estimate the global and regional responses to external forcing, to investigate covariation between future regional trends in precipitation and temperature and for comparison with projected temperature trends. The models utilized are listed in Table 1.

Questions have arisen regarding model interdependence (Knutti et al., 2013). Only minor differences were noted here when distributions were computed after first averaging over models within a family. The full multimodel set (one ensemble member per model) was therefore utilized.

2.3. Satellite data and reanalyses

In the present report we describe downscaling to the monthly time step; the possibility also exists of generating daily output, by resampling from a dataset such as AgMERRA, a product based on the MERRA reanalysis (Rienecker et al., 2011) developed for crop modeling as part of the international AgMIP project (http://agmip.org). This is discussed in Section 5.

2.4. Stratospheric ozone

Because stratospheric ozone may affect SESA precipitation we model a partial dependence. Both past and projected concentration data, as compiled by the Stratosphere–troposphere Processes And their Role in Climate (SPARC) activity of the World Climate Research Program (Cionni et al., 2011), are utilized. This dataset serves as a boundary forcing for the majority of CMIP5 models, which do not compute stratospheric ozone interactively.

3. Method

The procedure developed herein advances the work described in G12, in part by adding refinements but also though the representation of within-region variability in terms of principal components. This enables the consideration of larger, more climatically complex regions than could easily be accommodated using the earlier method. In common with G12, climate variability is decomposed into long-range trend, annual-to-decadal variability and subannual variations. The first two of these are modeled independently and the results combined, producing annually-resolved seasonal simulations over the entire gridded domain. These simulations are then downscaled in time, using a k-NN variant. In South Africa the

Table 1
Climate modeling centers and models.

Center	Country	Model ID
Commonwealth Scientific and Industrial Research Organization (CSIRO) and Bureau of Meteorology (BOM)	Australia	ACCESS1-0
–	Australia	ACCESS1-3
Beijing Climate Center (BCC), China Meteorological Administration	China	BCC-CMS1.1
–	China	BCC-CMS1.1(m)
College of Global Change and Earth System Science (GCESS), Beijing Normal University	China	BNU-ESM
Canadian Centre for Climate Modelling and Analysis (CCCMA)	Canada	CanESM2
National Center for Atmospheric Research (NCAR)	USA	CCSM4
Community Earth System Model Contributors (NSF-DOE-NCAR)	USA	CESM1-BGC
–	USA	CESM1-CAM5
Centro Euro-Mediterraneo per I Cambiamenti Climatici (CMCC)	Italy	CMCC-CESM
–	Italy	CMCC-CM
–	Italy	CMCC-CM5
Centre National de Recherches Météorologiques/Centre Européen de Recherche et Formation Avancée en Calcul Scientifique (CNRM-CERFACS)	France	CNRM-CM5
Commonwealth Scientific and Industrial Research Organization in collaboration with Queensland Climate Change Centre of Excellence (CSIRO-QCCCE)	Australia	CSIRO-Mk3.6.0
LASG, Institute of Atmospheric Physics, Chinese Academy of Sciences and CESS, Tsinghua University (LASG-CESS)	China	FGOALS-g2
The First Institute of Oceanography, SOA, China (FIO)	China	FIO-ESM
NOAA Geophysical Fluid Dynamics Laboratory (NOAA GFDL)	USA	GFDL-CM3
–	USA	GFDL-ESM2G
–	USA	GFDL-ESM2M
NASA Goddard Institute for Space Studies (NASA GISS)	USA	GISS-E2-H
–	USA	GISS-E2-R
Met Office Hadley Centre (MOHC)	UK	HadGEM2-CC
Met Office Hadley Centre (additional HadGEM2-ES realizations contributed by Instituto Nacional de Pesquisas Espaciais, INPE)	UK	HadGEM2-ES
Institute for Numerical Mathematics (INM)	Russia	INM-CM4
Institut Pierre-Simon Laplace (IPSL)	France	IPSL-CM5A-LR
–	France	IPSL-CM5A-MR
–	France	IPSL-CM5B-LR
Atmosphere and Ocean Research Institute (The University of Tokyo), National Institute for Environmental Studies, and Japan Agency for Marine-Earth Science and Technology (MIROC)	Japan	MIROC5
Japan Agency for Marine-Earth Science and Technology, Atmosphere and Ocean Research Institute (The University of Tokyo), and National Institute for Environmental Studies (MIROC)	Japan	MIROC-ESM
–	Japan	MIROC-ESM-CHEM
Max-Planck-Institut für Meteorologie (Max Planck Institute for Meteorology, MPI-M)	Germany	MPI-ESM-LR
Meteorological Research Institute (MRI)	Japan	MRI-CGCM3
Norwegian Climate Centre (NCC)	Norway	NorESM1-M
–	Norway	NorESM1-ME

model was fit to annual mean values of precipitation and maximum and minimum daily temperatures. Here we model the principal growing season, which we take as September–February (SONDJF). Out-of-season months are represented by climatological values, which for temperature are superimposed on a slowly-evolving trend bearing a fixed offset to the SONDJF trend.

A method flow chart appears as Fig. 2 in G12, regarding which there are two notable differences with the current implementation: The first involves the manner of projecting future trends, which here involves a balance of stratospheric ozone and global warming influences. The second concerns the representation of grid-scale variability in terms of principal components; in G12 regional means of the three principal variables were modeled directly. Further descriptive material may be found in that reference.

The technique inherits from the so-called "delta" method (Hay et al., 2000; Beldring et al., 2008), in which observed data sequences are superimposed on projected changes. Whereas the classical delta method is limited to the repetition of observed sequences, however, here the annual-to-decadal component is simulated, providing an essentially infinite variety of possible realizations. In the k-NN downscaling step, values are resampled from the observational record, so subannual sequences within individual years are drawn from those that have been observed. However, subannual values are also rescaled, additively for temperature, multiplicatively for precipitation, so as to bring seasonal means into agreement with the simulated values.

One other feature that differentiates the current scheme from other downscaling methods is the restriction of GCM information to regionally-averaged values. We are guided in this choice by the observation that GCMs are most reliable on continental to subcontinental scales (Masson and Knutti, 2011).

3.1. Detrending the observational record

The purpose of characterizing historical trends is to remove them, the residual variations then being passed to the annual-to-decadal modeling routine. Ideally, the abstracted trends would

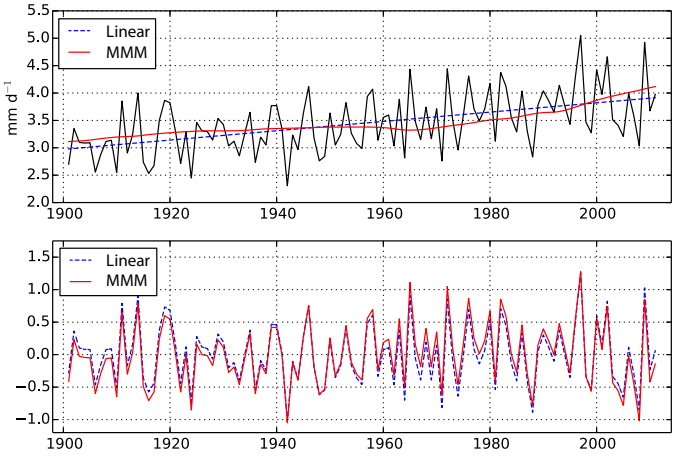

Fig. 2. (a) Two detrending methods applied to regional mean precipitation and (b) residuals from those methods. The latter are taken to represent natural annual-to-decadal variability.

represent the response to anthropogenic forcing, so that the differing model levels would apply not to differing time scales per se, but to variations mediated by different kinds of process. The simulated annual-to-decadal values would then maintain the characteristics of observed unforced variability, rather than some unknown mixture of the forced and the natural. Offline tests, conducted in the domain of GCMs, may then be used to infer potential cross-scale interaction (i.e., forced changes in the characteristics of "natural" variability), for incorporation in the simulation model.

To accomplish this separation we detrend by regressing the observed data, at the grid level and separately for each variable, on a global mean, multimodel mean (MMM) temperature record. In principle this procedure extracts that part of local variability that is linearly dependent on the primary index of anthropogenically-forced climate change (Greene et al., 2011). Analysis suggests that contributions from solar and volcanic forcings are relatively small by comparison and of opposite sign (Hegerl et al., 2003). The MMM signal is used in order to reduce the possible confounding effect of natural decadal variations: Among the different models such variations are incoherent and tend to cancel, leaving a common signal – the forced response to the imposed boundary conditions that the models share. Although stratospheric ozone may also play a role in modulating SESA precipitation, the ozone and temperature signals during the 20th century are essentially collinear to within sign, so nothing is gained by inclusion of the former.

The MMM signal is concave up, increasing more rapidly toward the end of the record, and will provide a better fit to predictands that behave in like manner, particularly temperature. Since precipitation trends tend to be small when compared with year-to-year variations, differences resulting from the two detrending methods will also tend to be small, and because we consider the MMM method preferable from the conceptual standpoint we employ it here. The difference in fitted trend and residual signal is illustrated in Fig. 2, the two methods being applied here to the SESA regional mean precipitation record. Conceptually, the residual from MMM detrending represents natural, or unforced variability; it is this signal, for all three variables (at the gridbox level and following data reduction via PCA) that is passed to the statistical model for annual-to-decadal variations.

3.2. Interannual-to-decadal variability

The resultant of the detrending step is seasonally-resolved data, i.e., having one value per year representing the SONDJF mean, at each gridbox for each of the primary variables. These data, which now have zero time means, represent the natural component of climate variability. After data reduction, a subset of leading principal components is fit with a statistical model, which is then used to generate a long stream of simulated data. After back-conversion into the primary climate fields, a selected slice of this data is then post-processed to yield the annual-to-decadal variability component of the simulation.

3.2.1. Data reduction in terms of PCA

The SESA domain has an area of about 4.2×10^6 km^2 and, at a resolution of 0.5°, comprises 734 land grid boxes, giving it an areal extent more than an order of magnitude greater than that considered in G12. In that work it was shown that annual-to-decadal variability was rather homogeneous across the domain. Modeling was performed directly on the regionally-averaged primary variables and simulated sequences broadcast to localities via linear regression. Here, by contrast, we prefilter the data in terms of empirical orthogonal functions (EOFs), retaining a subset of the leading patterns. The principal component time series (PCs) for these patterns are then modeled and simulated. No broadcasting step is then necessary, since the simulated PCs can be immediately transformed back into seasonal variations over the entire domain.

Fig. 3 shows the first five multivariable EOFs, along with the corresponding PC time series. These are obtained by first standardizing the three variables, then combining them into a single large data matrix on which the EOF analysis is performed, here using singular value decomposition. The EOFs are scaled so as to be orthonormal, the squared singular values then representing the PC variances. These five EOFs explain 25.6%, 22.3%, 7.3%, 7.2% and 5.1% of the variance, respectively, in the multivariate data.

Fig. 3 indicates that precipitation and temperature tend to vary inversely, with the relationship somewhat more consistent for Tmax than Tmin. This may be because the cloudiness associated with precipitation is more effective in reducing surface incoming shortwave radiation during the day than are nocturnal clouds in reducing outgoing longwave radiation. A moist surface also partitions surface fluxes in favor of latent, rather than sensible heat. Inverse patterns of precipitation and Tmax are clearly visible in all of the EOFs. Tmax and Tmin can also be seen to covary in the positive sense, Tmax thus coupling more strongly with both precipitation and Tmin than those variables with each other. Validation exercises (see Section 4) indicate that in order to preserve grid-level statistics a larger number of EOFs must be retained than might be the case for classical diagnostic studies. Based on those exercises it was decided to retain the 20 leading modes for these simulations.

3.2.2. Vector autoregressive (VAR) model

As in G12 we utilize a first-order vector autoregressive (VAR) model for annual-to-decadal variations, but here fit to the retained PCs. Global wavelet spectra of the observational time series do not differ significantly (at $\alpha = 0.1$) from red noise, while information tests offer no justification for the use of higher-order models.

The VAR(1) model can be written

$$\mathbf{Y}_t = \mathbf{A}\mathbf{Y}_{t-1} + \boldsymbol{\epsilon}_t, \quad (1)$$

where $\mathbf{Y}_t$ is the N-component PC vector at time (i.e., year) t, $\mathbf{Y}_{t-1}$ its lagged value one year previous and $\boldsymbol{\epsilon}_t$ a random, vector noise process that is uncorrelated in time but may be correlated across PCs. Note that while the PCs themselves are uncorrelated by construction, this need not be the case for the terms on the rhs of (1) considered separately. The $N \times N$ matrix $\mathbf{A}$ holds the coefficients relating $\mathbf{Y}_t$ to its predecessor one time step previous, its N^2 elements characterizing lag-1 relationships between the N^2 possible pairwise combinations of PCs, thus including serial autocorrelation as well as lag-1 cross-correlations.

The model is fit using the Dynamical Systems Estimation (dse) package (Gilbert, 1995) in the "R" programming language (Ihaka and Gentleman, 1996), then utilized to generate a single, long (12 kyr) simulation sequence, which is then transformed back into the primary variable space, with the standardization and area-weighting removed. In a postprocessing step this long series is screened, then sliced, in order to provide an example sequence of annual-to-decadal variability having specified deviations during a particular future decade. Superimposing this data slice on the projected trends provides a way to assess relative contributions from forced and natural variations during that decade.

3.3. Specification of future trends

For the past, detrending is important inasmuch as it determines the residual data passed to the annual-to-decadal modeling stage and thus the character of future variability. The specification of future trends, on the other hand, concerns the delineation of uncertainty, based on our current understanding of potentially compensating driving factors in SESA.

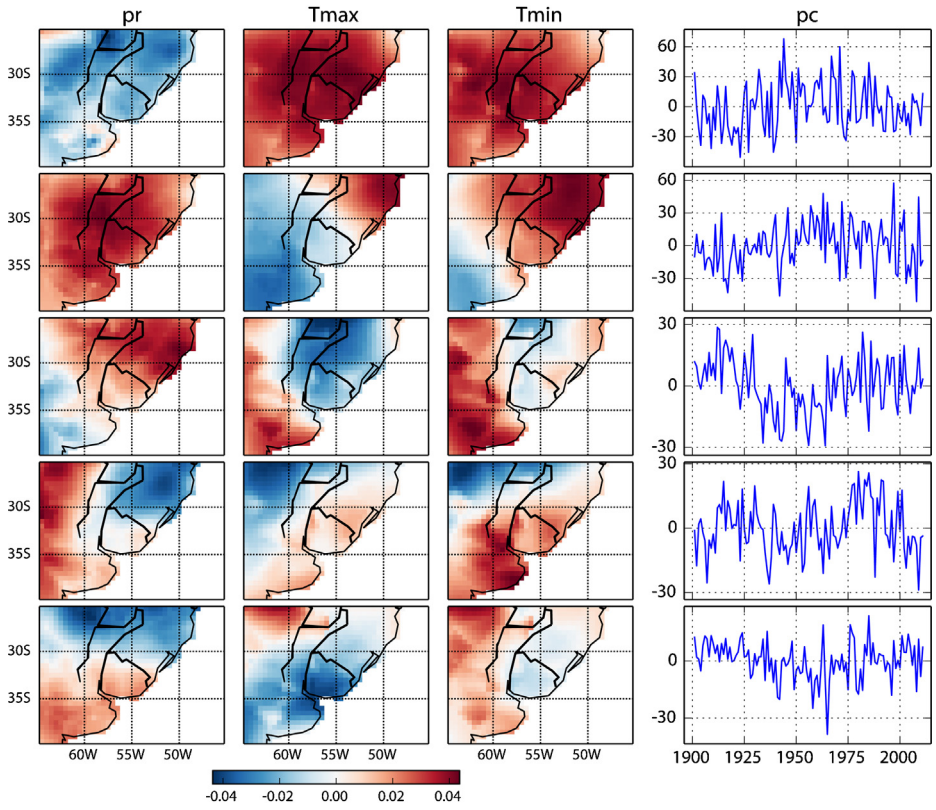

Fig. 3. The first five EOFs and corresponding PCs (rows 1–5) in a decomposition of the detrended 1901–2011 seasonal climate record for SESA. Since the plots in each row represent the same EOF pattern, colors have been kept consistent across the precipitation and temperature variables.

3.3.1. Role of stratospheric ozone

In the multimodel mean, GCMs of the CMIP5 family underestimate the observed upward tendency in 20th-century SESA precipitation by a factor of more than five (Seager et al., 2010; Gonzalez et al., 2014); it would therefore seem unwise to depend on those models for quantitative estimates of future long-range trends. Additionally, the late 20th-century depletion of stratospheric ozone has been implicated as a possible driver of the increase in SESA summer rainfall, owing to its cooling effect on the lower stratosphere and the consequent spinup of the Antarctic polar vortex (Kang et al., 2011; Gonzalez et al., 2014). Inadequate GCM representation of processes governing the evolution of stratospheric ozone and/or its consequent radiative and dynamical effects may contribute to the difficulty in simulating SESA precipitation trends.

3.3.2. A balance of two influences

For the above reasons the GCMs are utilized only indirectly in specifying a future long-range precipitation trend. Rather, it is assumed that there are two dominant influences on the future tendency, namely, changes in stratospheric ozone and warming of the planet owing to increasing atmospheric greenhouse gas (GHG) concentrations, whose relative importance in driving future precipitation changes is unknown. These driving factors are used as predictors, using SPARC ozone data and simulated MMM global mean temperature records from the GCMs, respectively. For the former, we take the zonal mean ozone concentration for Sep–Nov (SON), averaged over 70–90° S and integrated from 100 to 300 mb. SON represents Southern Hemisphere spring, the time of year when a combination of still-cold stratospheric temperatures and increasing shortwave radiation facilitate ozone destruction

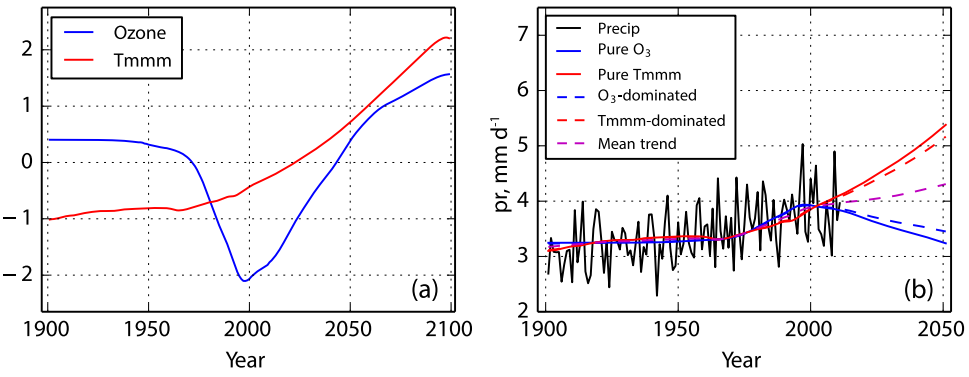

Fig. 4. (a) South Polar stratospheric ozone, from the SPARC database, and a multimodel mean temperature record. Both series have been standardized. (b) Regression of the regional SONDJF precipitation record on each of the signals shown in panel (a), along with weighted projections. See text for details.

(Solomon, 1999), leading to the development of the well-known "ozone hole." For the temperature predictor, which to first order represents the planetary response to GHG forcing, we construct a multimodel-mean, global mean signal, as described in G12. The multimodel mean signal is also smoothed using a lowpass Butterworth filter having a half-power point at a frequency of 0.1 yr^{-1}. The two predictors, standardized for comparison, are shown in Fig. 4a.

Owing to the lack of small-scale features in these signals, as well as their similar (if inverted) shapes during the 20th century, they cannot be combined as predictors in a multivariate regression. Rather, they are treated separately and the results then combined. Fig. 4b shows fitted trendlines from individual univariate regressions on the two predictors, as well as future projections based on the respective inferred sensitivities. For the latter, several variants are illustrated, based on weighting the individual trends toward one predictand or the other. If the ozone record is used alone, the future trend labeled "Pure O_3" is obtained, and similarly for the MMM temperature signal ("Pure Tmmm"). The other trend projections show weights for Tmmm and ozone of (0.1, 0.9), (0.9, 0.1) and (0.5, 0.5), for "O_3-dominated", "Tmmm-dominated" and "Mean trend", respectively. The true balance between these two factors in controlling the future evolution of SESA precipitation is unknown; the range of possibilities spanned by the alternatives shown mirrors this uncertainty. In the generation of simulations we sample from the distribution represented by this spread, at the values represented in Fig. 4b by dashed lines.

3.3.3. Prediction error

In addition to the uncertainty in the forced response represented by the spread in future trends shown in Fig. 4b there will be prediction error associated with uncertainty in the estimated regression coefficients. Tests suggest that this uncertainty is not negligible, but is relatively small compared with the basic trend uncertainty represented in the figure. Limitation in forward projection to just a few decades implies that projected trends will not extend far outside the dynamic range of the observations used to estimate them.

3.3.4. Out-of-season values

The trends shown in Fig. 4 are applied, as noted, to SONDJF means. We model seasonal, rather than annual mean values in order to increase the signal-to-noise ratio in the training data, and because the growing season is of primary importance for agricultural applications. Because crop models may be run sequentially over a span of years, or initialized prior to the start of the growing season, however, we also provide for those months that fall outside the nominal growing period. This is done by first computing a climatology for the months in question, for each of the three model variables. For precipitation this climatology is utilized directly to represent out-of-season values; for temperature, the centered climatology pattern is superimposed on a trend that is offset from the growing-season trend by the mean observed temperature difference between the two seasons. This is done at each gridpoint, and insures, as climate warms, against increasingly large discontinuities between the growing season and what otherwise would be static climatological temperatures for the rest of the year. Out-of-season precipitation has not been observed to trend during the observational period, and would not be expected to respond to ozone variations, which are marked by a distinct seasonal fingerprint (Son et al., 2009).

3.3.5. Fractional precipitation treatment

It proves advantageous to represent precipitation in terms of its logarithm, so that future changes can be expressed in fractional, rather than absolute terms. The future trend is computed at the regional scale, as per the balance described in Section 3.3.1, and is taken as a best estimate for all gridpoints. A modeling option is provided to add a local perturbation, based on grid-level 20th-century behavior, to the regional mean value. Invoking this option would induce some scatter into the gridbox-level trends, providing more realistic simulation results in the case where modeled agricultural yields are aggregated over a subregion of significant areal extent.

3.3.6. Temperature trends

Tmax and Tmin are treated as separate (not necessarily independent) variables, with respect to both trends and annual-to-decadal variations. Both are detrended at the grid level, by regression on the same MMM signal utilized as a predictor in the treatment of precipitation. The resulting coefficients, which are then utilized to project temperatures forward, represent ratios of local to global temperature change. For the region as a whole the coefficients for Tmax and Tmin are 0.61 and 1.13, respectively, indicating that during the 20th century Tmin has increased twice as rapidly as Tmax, relative to global mean temperature. As with precipitation, the initially-specified future temperature trends are everywhere uniform, with the option to add a local perturbation based on grid-level 20th-century behavior. This allows some variation from grid to grid while controlling the overall dispersion of trends, mimicking the natural smoothing of horizontal temperature gradients by local circulations.

It may be asked why the regional MMM temperature trend is not simply utilized directly, rather than projecting a regional trend based on the observed dependence on global mean temperature. Fig. 5 compares the two methods, as applied to the mean temperature. The future MMM temperature is seen to follow a trajectory that is quite similar to (if slightly more linear than) that of the trend projected using the 20th-century regression. However the former exhibits an additive bias with respect to the observed, of about 0.9° C. After removing this bias the future trend would be quite similar for both methods.

Another question that might be posed regards possible covariation of future precipitation and temperature trends. We include provision for this in the general model, but in SESA, other than for a small group of relative outliers (six out of the 34 models polled), there is no significant relationship between future regional trends in temperature and precipitation (not shown). We therefore do not adjust future temperature trends based on the specified balance between ozone and temperature influences.

3.4. Cross-scale coupling

It has been hypothesized that precipitation variability will increase with global temperatures, owing to the increase in water saturation vapor pressure with temperature (see, e.g., FAQ 3.2, p. 262 in Solomon et al., 2007). This is tested for the interannual time scale in Fig. 6. Fig. 6a shows a histogram of the ratio of interannual precipitation variance for 2040–2059 to that of 2006–2025, the distribution being across the CMIP5 ensemble enumerated in Table 1. The distribution is skewed, with a small number of models showing a substantial increase but most of the population nearer the low end of the scale. The median variance ratio is 1.04. In Fig. 6b the values from panel (a) are plotted against each model's global mean temperature change between the same two periods, to test whether models that warm more exhibit greater variance increases. The evidence here is also inconclusive, with linear regression yielding a positive, but not statistically significant slope. In the simulation model, interannual variability can be scaled by global mean temperature change, but in view of these results it was decided not to implement this procedure for SESA.

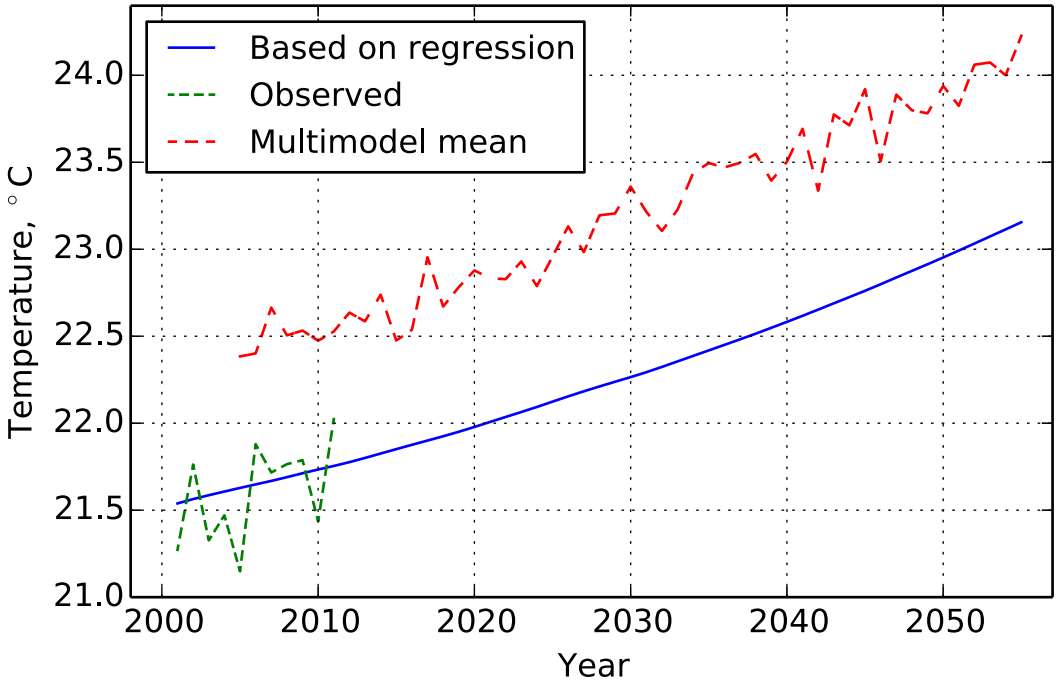

Fig. 5. Regional mean temperature, projected forward by regression on the MMM temperature record and in the CMIP5 multimodel ensemble mean. The observed SESA record from 2001–2011 is also shown.

3.5. *Assembling the seasonally-resolved signal*

Future trends, developed as in Section 3.3 and gridbox-level variability on the annual-to-decadal level, simulated as described in Section 3.2, are now combined. The regional precipitation trend is computed based on the specified balance factor f, while the annual-to-decadal component is sliced from the very long simulation sequence generated by the VAR model.

The long sequence consists effectively of many realizations of decadal-length climate variability, from which we may choose according to any criteria of interest. Because we are interested in the decadal scale, we screen the long sequence for decades in which regional mean precipitation lies at or near a defined percentile. To efficiently explore the range of decadal uncertainty we choose three levels, namely the 5th, 50th and 95th percentiles. We combine these with three levels for the precipitation trend balance factor f: 0.1 (ozone-dominated), 0.5 (equal ozone and warming effects) and 0.9 (GHG-dominated) spanning the trend uncertainty range. Combining each trend variant with the three decadal fluctuation percentiles yields a basic simulation ensemble having nine members.

On the annual-to-decadal scale, the three fields exhibit large-spatial-scale covariance (Section 3.2.1). In screening the long simulation sequence for a dry decade, for example, the expectation would be that mean temperatures for that decade would be above normal. However for a given realization the temperature variable could fall anywhere within its conditional range. A secondary level of screening is thus conducted in order to insure that Tmax and Tmin lie reasonably close ($\pm 0.5\sigma$) to their conditional means, given the specified precipitation level, in effect selecting for subsequences that are "jointly typical," in the information-theoretic sense (Cover and Thomas, 2006). A fourth screening requires the precipitation deviation for the previous decade to be $<1\sigma$, so as to minimize potential initial-state bias. Specification of these criteria is up to the investigator; the primary screening could be for a specified fluctuation in temperature rather than precipitation, for example.

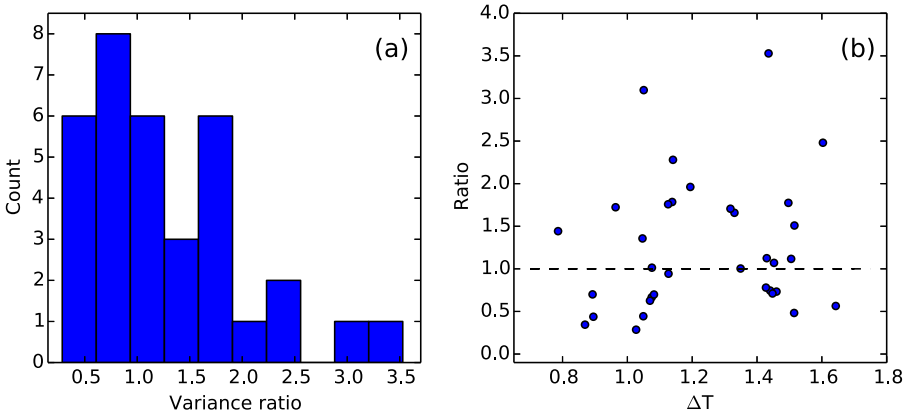

Fig. 6. (a) Histogram of the ratio of interannual SESA precipitation variance for 2080–2099 to that of 2006–2025. Distribution is over the models listed in Table 1, for the RCP8.5 scenario. (b) The values in panel (a) plotted against global temperature change between the same two periods. Dashed line in (b) is plotted at $y = 1$.

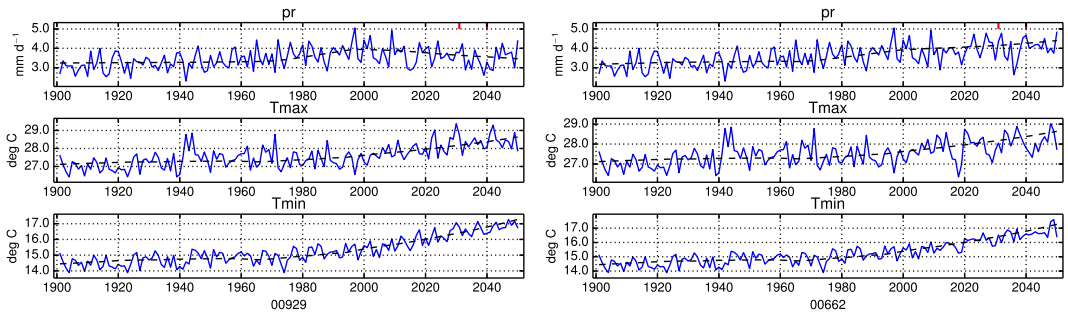

(a) Ozone-dominated ($f = 0.1$) (b) Equal influence ($f = 0.5$)

Fig. 7. Simulation examples, showing regional mean, seasonal (SONDJF) mean time series of the principal variables. Decadal precipitation fluctuations at the fifth percentile occur at years 2031–2040, demarcated by short vertical bars in the topmost plots. Dashed lines represent trends.

Fig. 7 provides two examples of final simulation sequences, presented as regional mean, seasonal mean time series. In Fig. 7a the balance factor f has been specified so as to allow the influence of ozone recovery to dominate; consequently, future precipitation undergoes a gradual decline. In Fig. 7b the factor f is set at 0.5, so ozone and GHG influences are nominally equal. As in Fig. 4b this produces a positive future precipitation trend, albeit weaker than that characterizing the late 20th century. A more sharply increasing trend results if f is specified so that GHG forcing dominates.

On each of the trends shown in Fig. 7 has been superimposed a sequence from the long simulation, screened for decadal-mean precipitation fluctuations lying near the fifth percentile; the long simulation has been sliced so that these fluctuations occur during the 2031–2040 decade. Inspection of the figure reveals differences in detail within this decade, to which agricultural or economic outcomes might possibly prove sensitive. In such a case it may be sensible to focus on a single combination of trend and decadal fluctuation, exploring the range of effects produced by an ensemble of simulations having varying intradecadal patterns. Fig. 7 is presented simply as an illustration of the range of available scenario control.

The data through year 2011 shown in Fig. 7 consist of the actual observational record (cf. the two panels), showing the ability of the simulation model to capture the characteristics of the training data to which it is fit. We visit this subject in more detail in Section 4

4. Validation and diagnostics

For validation purposes it must be kept in mind that the simulated annual-to-decadal sequences are not intended to be predictive, in the sense that specific year-to-year or decadal-to-decade variations are forecast. Rather, the simulations are designed to explore future uncertainty ranges, given our knowledge of past variability and likely future influences. Validation in this case takes the form of comparison statistics.

4.1. Regional level

Table 2 compares the covariance matrix for the regionally averaged, detrended observations with that for the long simulation sequence for balance factor 0.5, reconstructed using 20 EOFs. (The values change slightly with f.) The Table shows that the simulations replicate fairly accurately the observational covariance. A particular slice of length 39 yr, the length of the synthetic portion of the simulation, will of course exhibit deviations from these values owing to sampling variability.

A second temporal characteristic of interest is persistence, or serial autocorrelation, in the individual variables, for which observed and simulated values, computed similarly, are shown in Table 3. The observational values are replicated by the simulation to well within their uncertainty ranges.

Table 2
Covariance matrices for the regional observations and long simulation sequence.

	Observations			Simulation		
	pr	Tmax	Tmin	pr	Tmax	Tmin
pr	0.224			0.225		
Tmax	−0.084	0.237		−0.084	0.234	
Tmin	0.025	0.110	0.155	0.025	0.108	0.154

4.2. Gridbox level

The EOF decomposition serves both to illuminate regional patterns of variability (Fig. 3) and as a means of encoding variation at the gridbox level. We focus here on the latter aspect as a function of the number of retained modes.

4.2.1. Variance replacement

Since only a subset of leading patterns is used, the raw data generated the VAR model will generally be variance-deficient. The assumption is that the leading EOFs represent signal and the remainder noise, as far as the simulation properties of interest are concerned. The variance deficit is therefore corrected, at the gridbox level, by adding uncorrelated noise to the raw simulation values. Fig. 8 illustrates this procedure, using the precipitation field from a 20-EOF simulation. Fig. 8a shows the ratio of observed to simulated variance for the raw simulation data. The 20 PCs utilized represent only about 90% of the data variance, and at every gridbox the ratio of observed to simulated variance is greater than unity, with values ranging as high as two.

The added noise variance at each grid is set equal to the difference between observed and simulated values, bringing the latter into agreement with the former to within a random covariance term. The result can be seen in Fig. 8b, where the checkerboard pattern reflects slight mismatches due to this term. Note that the large discrepancies of Fig. 8a have been replaced, in the corrected field, by much smaller deviations. One can also see, for example, that in the region lying approximately between 25–30° S and 50–55° W, where the variance deficit was initially small, the applied corrections and resulting random deviations are also small. We conclude

Table 3
Lag-1 autocorrelation coefficients for pr, Tmax, Tmin, for the regionally-averaged observations and long simulation.

Source	pr	Tmax	Tmin
Observations	−0.070	0.155	0.143
Simulation	−0.064	0.165	0.146

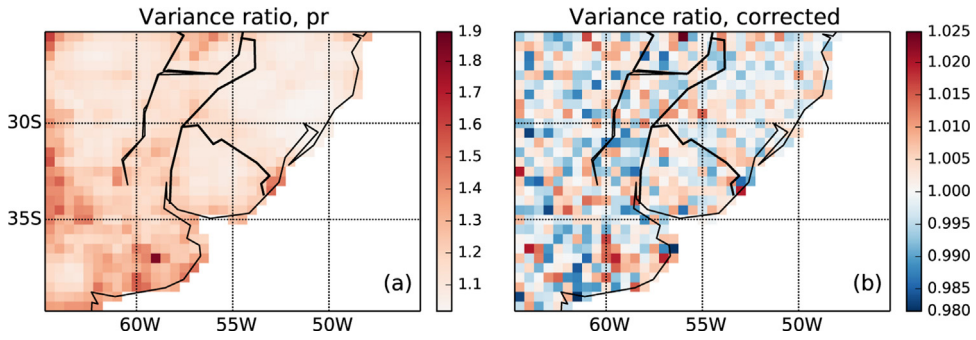

Fig. 8. Ratio of observed to simulated grid-level variance, shown here for precipitation, (a) prior to variance correction, (b) after correction.

that this correction conserves observational variance patterns reasonably well.

4.2.2. Point-to-point correlations

Fig. 9 compares gridbox-to-gridbox seasonal correlations in the observed precipitation fields with those of simulations using 10, 20, 30 and 40 EOFs, with the comparison made before and after the variance correction (top and bottom rows, respectively). The data have been thinned for clarity.

Reproduction of these correlations is generally quite good, even for $N = 10$ EOFs, although it does improve as N increases (reading from left to right in each row). Variance correction, on the other hand (reading from top to bottom in each column), has very little influence. The difference is clarified if we think of EOF additions and variance correction as adding signal and noise, respectively, to the simulated field.

Fig. 9 is representative of results obtained for Tmax and Tmin, although somewhat less improvement, relatively speaking, is seen in going from $N = 10$ to $N = 20$ with those variables. Based on these comparisons, particularly the more notable improvement in precipitation correlations in going from Figs. 9a and e to b and f, respectively, the value $N = 20$ has been utilized for the simulations discussed herein. Clearly there is some latitude in this choice, which will depend on the agricultural modeling strategy adopted.

4.2.3. Additional comparisons

Point-to-point comparisons were also made of intervariable correlations and serial autocorrelation in individual variables. Both improve with the inclusion of additional EOFs, although the latter is less sensitive to variance correction. Since EOFs by construction maximize spatial covariance, and since the multivariate analysis treats the different variables as if they were additional spatial coordinates, this result is not unexpected.

5. Temporal downscaling

A final step in simulation generation is temporal downscaling, here to monthly resolution; daily output is then generated in a post-processing step, described in Section 6. The downscaling scheme is the same modified k-NN method as employed in G12 (Rajagopalan and Lall, 1999), and consists of searching within the observational record for a small number, k, of distinct years whose regional climate means, expressed as three-vectors with components precipitation, Tmax, Tmin, are closest, in terms of a probabilistic metric,

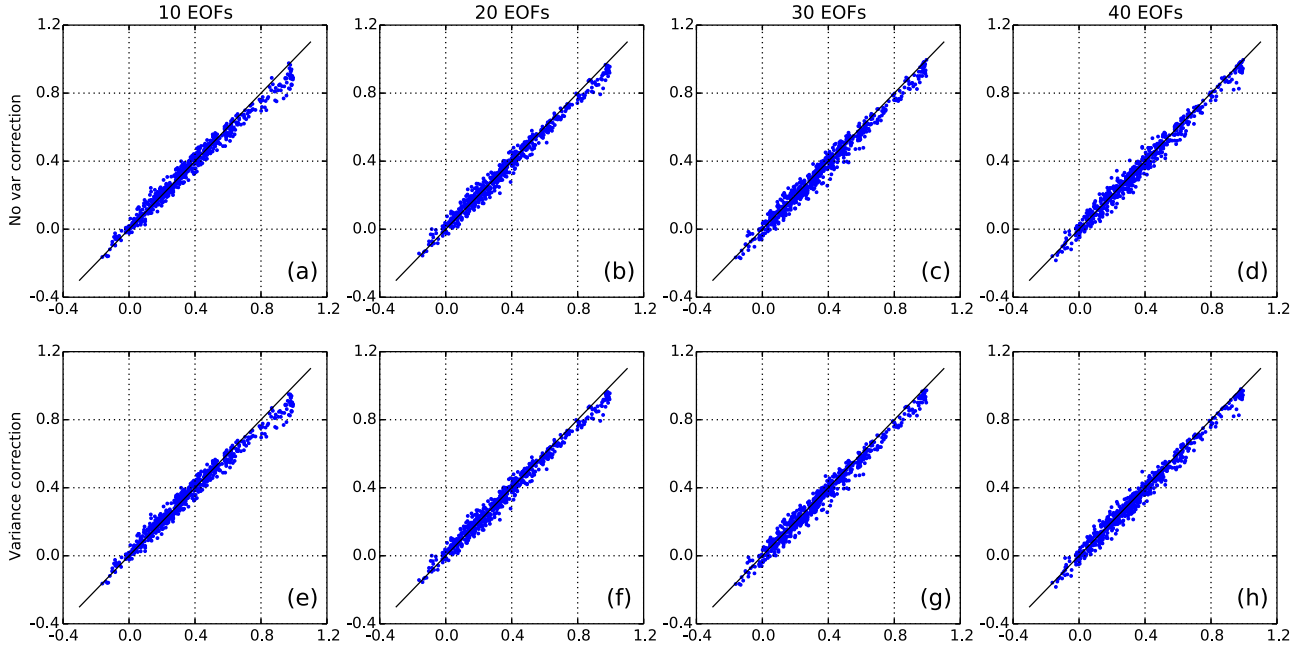

Fig. 9. Point-to-point seasonal precipitation correlations for 10-, 20-, 30- and 40-EOF simulations, plotted against observational values. Panels (a)–(d) show data prior to variance correction, (e)–(h) afterward. The data have been thinned for readability.

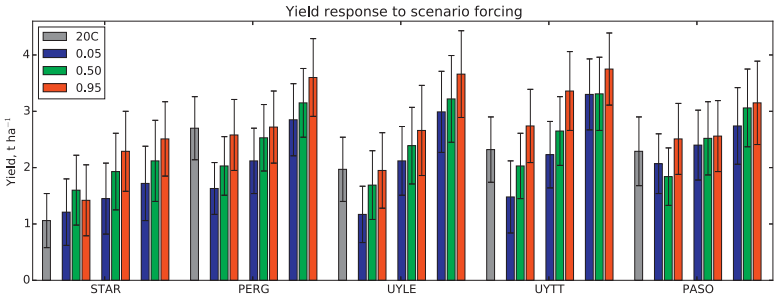

Fig. 10. Soybean yields at each of the stations for the 9-member basic simulation ensemble. For each station a gray bar shows mean simulated 20th-century yields; this is followed by results for 2031–2040, collected into three groups. These correspond, from left to right, to balance factors $f = 0.1$, 0.5 and 0.9. Bars within each group show yields associated with decadal precipitation fluctuations lying at the 5th, 50th and 95th percentiles, as shown in the legend. Error bars show $\pm 1\sigma$, pooled across years and weather generator realizations.

the Mahalanobis distance (Mahalanobis, 1936), to the vector of the year being simulated. A weighted random selection among the k candidates is made, and the monthly values of the selected year are then nudged so that their vector mean agrees with that simulated. This nudging is performed multiplicatively for precipitation, additively for the temperature variables. The k-NN method mimics those dependencies that are present in the observational data: For example, if, during a wet year, precipitation tends to occur preferentially in the late summer, this attribute will be carried over to the simulations. The downscaling to daily values in G12 was found to reproduce dependencies of wet and dry spells as well as 3-day wet extremes. The use of $k = 5$ here is common with G12.

Seasonal output may be downscaled directly to the daily time step through the use of AgMERRA. This bypasses the weather generator step and permits the inclusion of additional agriculturally-relevant variables, including insolation, dew point, vapor pressure and wind speed. Use of the weather generator, on the other hand, permits more rapid generation of many realizations of daily variability.

6. Soybean yield simulations

The Hansen and Ines (2005) weather generator was used to create, for each scenario in the nine-member basic ensemble, 100 realizations of daily weather sequences, for five station locations along a transect extending from 37° S, 64° W to 28° S, 52° W (Table 4). The transect originates in Argentina in the southwest, passes through Uruguay and terminates in Brazil in the northeast, sampling a range of climatologies. Simulations from the three gridboxes nearest each station were downscaled, using station-specific parameter sets. In addition to daily values of precipitation, Tmax and Tmin, the weather generator also simulates solar radiation, based on distinct station climatologies for wet and dry days.

Yield simulations using the soybean crop model in DSSAT-CSM (Jones et al., 2003) were then run for each of the downscaled scenarios, using soil properties and a cultivar suggested by local partners in the region. For each scenario, yields were averaged over the three gridbox-level simulations at each location. Since the cultivar is static, the modeled yield anomalies represent responses only to climate variations.

Fig. 10 shows simulated yields at each of the stations for the 20th century (1951–2000) and for each of the nine scenarios. The latter represent the 2031–2040 period, during which specified decadal precipitation fluctuations occur. For each station three groups of bars are shown, corresponding to trend scenarios having balance factors $f = 0.1$, 0.5 and 0.9, reading from left to right. The three bars within each group correspond to decadal precipitation fluctuations at the 5th, 50th and 95th percentiles, as indicated in the figure legend. Thus the progression from left to right is from dryer to wetter, both among and within groups.

The broad implications of Fig. 10 are clear. As future precipitation trends, represented by f, increase, yields increase as well, at all of the stations. For a given trend, yields during the test period are then modulated by the specified decadal fluctuations, with wetter decades corresponding to higher yields and vice versa. Responses to the fluctuations are a little noisier than those associated with the trend variations, with stations STAR and PASO showing non-monotonic yield shifts as the test decade becomes wetter, for $f = 0.1$, a scenario characterized by long-term drying (see Fig. 4b). The $\pm 1\sigma$ error bars illustrate the importance of using a large simulation ensemble, to reveal the common underlying response at each of the stations.

For most of the stations the mean simulated 20th-century response falls within the range of 21st-century simulations. Given that the second half of the 20th century saw the full range of stratospheric ozone levels (Fig. 4a), with depletion beginning after midcentury and recovery shortly before year 2000, this may not be a surprising result. Only for station STAR is the 20th-century yield lower than any of the future values, perhaps reflecting the fact that STAR is climatologically the driest of the locations (Table 4).

A saturation-like response to increasing precipitation was identified by Podestá et al. (1999) for soybean yields in central-eastern Argentina, in an analysis based on interannual yield variations and the first principal component of the precipitation field over a group of stations. Many differences in treatment render a direct comparison with that result infeasible, but the preliminary crop modeling results presented here certainly merit further investigation; this will be undertaken in a separate publication.

A comparison of yield responses to differences in trend, with those attributable to decadal fluctuations, appears in the two rightmost columns of Table 4, which show standard deviations taken over trends (averaging the three fluctuation values for each trend value) and across fluctuations (vice versa), for each of the stations. The table shows that for the 2031–2040 period, using the computed distributions and the selected quantiles, variations in trend have a greater influence on yields than do decadal fluctuations. For earlier

Table 4
From left, the table shows station names and codes, countries, coordinates (latitudes in degrees south, longitudes in degrees west), mean SONDJF precipitation (mm d^{-1}) and standard deviations for simulated yields across trends and decadal fluctuations (σ_T and σ_F, respectively, t ha^{-1}).

Station	Code	Country	Lat	Lon	pr	σ_T	σ_F
Santa Rosa	STAR	Argentina	36.6	64.3	2.7	0.29	0.26
Pergamino	PERG	Argentina	33.6	60.3	3.5	0.47	0.31
La Estanzuela	UYLE	Uruguay	34.2	57.4	3.5	0.69	0.27
Trenta y Tress	UYTT	Uruguay	33.2	54.3	3.7	0.56	0.39
Paso Fundo	PASO	Brazil	28.2	52.4	5.4	0.35	0.15

decades in the 21st century the relative effects of trend would be reduced, compared with those of the fluctuations.

7. Discussion

In the foregoing we have tried to give both an overview of the modeling scheme and a sense of the many details that must be considered it its actualization. Although it may appear somewhat complex, method design has nonetheless been guided by the principle of parsimony, with the inclusion of only that level of detail necessary to insure that simulated variability bears a reasonable resemblance to that observed, and providing a defensible representation of uncertainty in our knowledge of future climatic changes.

The procedure described bears some resemblance to the delta method but goes beyond it, in the generation of synthetic variability rather than the reuse of observed sequences, in the layering of multiple time scales and in the reliance on CMIP5 for future distributions, rather than the use of arbitrary delta values. Synthetic annual streamflow sequences for the Colorado River were generated by Prairie et al. (2008) using a hidden Markov model (Hughes et al., 1999) for streamflow state and k-NN resampling for flow amplitudes. This was a univariate setting and the model did not address climate change, but the generation of synthetic data based on observations (in this case, paleodata) is common with our approach.

There is a substantial literature on statistical downscaling, the synthesis of which lies beyond the scope of this report (see Wilks and Wilby, 1999, for a review). At the annual-to-decadal level the present method functions something like a weather generator, producing sequences having the statistics of observed variability. Yet the incorporation of multiple time scales and their interactions makes it an intrinsically more complex scheme. We are not aware of other statistical downscaling methods that encompass this degree of multilevel complexity, or that make use of a similar amalgam of model and observational data.

8. Summary and conclusions

We have described a methodology for the stochastic generation of future climate sequences over the SESA region. These sequences extend out to a few decades in the future and include realizations of annual-to-decadal variability as well as climate-change trends. The data is downscaled to monthly resolution and for the purposes of crop modeling further disaggregated to daily; direct downscaling to the daily time step was discussed.

It is hypothesized that the two principal drivers of future precipitation trends in SESA are increasing greenhouse gases and stratospheric ozone recovery. Uncertainty regarding the relative effectiveness of these opposing influences is accounted for by the provision of a factor f, by which a particular future balance can be specified. Variations in f produce a range of trends spanning both signs.

Trends in both precipitation and temperature are specified on the regional level. In broadcasting these trends to the gridbox scale, parameters are introduced by which grid-level trends are permitted to scatter around the regional mean. These parameters permit a reasonable degree of grid-level variation, based on observed behavior, while, in the case of temperature, limiting the growth of potentially unrealistic horizontal gradients.

Variability on the annual-to-decadal scale is generated by a first-order vector autoregressive model fit to the detrended observational data, which is first prefiltered in terms of principal components. Twenty modes are utilized, based on an assessment of grid-level simulation statistics. Segments for individual simulations are sliced from a long sequence of effectively unlimited length according to several screening criteria, which select for a decade in which precipitation lies near a specified quantile while the temperature variables lie near their conditional means, given the specified precipitation level. Simulation sequences are variance-corrected in order to bring grid-level statistics into agreement with observed. The final sequences, here spanning 1901–2050, are downscaled to monthly time resolution using a k-NN variant.

Preliminary results using the agricultural model DSSAT-CSM show that, for the near-term at least, precipitation seems to play a dominant role in yield variations, non-climatic factors assumed constant. Local variations from grid to grid, and from realization to realization, speak to the importance of ensemble simulations, which can aid in delineating both the mean response and the expected spread on a range of time and space scales.

It is hoped that the simulations discussed herein, by providing a set of plausible future climate trajectories whose uncertainties may be quantified, will prove useful in delineating climate risks and possibilities for SESA on near-term time horizons.

Acknowledgments

We would like to thank the many colleagues at IRI and L-DEO, as well as an anonymous reviewer, who provided helpful suggestions and comments during the development of this work. We acknowledge the World Climate Research Programme's Working Group on Coupled Modelling, which is responsible for CMIP, and we thank the climate modeling groups (listed in Table 1 of this paper) for producing and making available their model output. For CMIP the U.S. Department of Energy's Program for Climate Model Diagnosis and Intercomparison provides coordinating support and led development of software infrastructure in partnership with the Global Organization for Earth System Science Portals. This research was funded by NSF EaSM award 1049066 (Multiscale Climate Information for Agricultural Planning in Southeastern South America for Coming Decades), with additional support for Greene and Chryssanthacopoulos provided by the U.S. Agency for International Development Climate Change Resilient Development program, under Contract No. EPP-I-00-04-00024.

References

Beldring, S., Engen-Skaugen, T., Foerland, E.J., Roald, L.A., 2008. Climate change impacts on hydrological processes in Norway based on two methods for transferring regional climate model results to meteorological station sites. Tellus 60A, 439–450.

Cionni, I., Eyring, V., Lamarque, J.F., Randel, W.J., Stevenson, D.S., Wu, F., Bodeker, G.E., Shepherd, T.G., Shindell, D.T., Waugh, D.W., 2011. Ozone database in support of CMIP5 simulations: results and corresponding radiative forcing. Atmos. Chem. Phys. Discuss. 11, 10875–10933.

Cover, T.M., Thomas, J.A., 2006. Elements of Information Theory. Wiley, Hoboken.

Gilbert, P.D., 1995. Combining VAR estimation and state space model reduction for simple good predictions. J. Forecasting 14, 229–250, Special Issue on VAR Modelling.

Goddard, L., Kumar, A., Solomon, A., Smith, D., Boer, G., Gonzalez, P., Kharin, V., Merryfield, W., Deser, C., Mason, S.J., Kirtman, B.P., Msadek, R., Sutton, R., Hawkins, E., Fricker, T., Hegerl, G., Ferro, C., Stephenson, D., Meehl, G., Stockdale, T., Burgman, R., Greene, A.M., Kushnir, Y., Newman, M., Carton, J., Fukumori, I., Delworth, T., 2013. A verification framework for interannual-to-decadal predictions experiments. Clim. Dyn. 40 (1–2), 245–272.

Gonzalez, P.L.M., Goddard, L., Greene, A.M., 2013. Twentieth-century summer precipitation in south eastern South America: comparison of gridded and station data. Int. J. Climatol. 33 (13), 2923–2928.

Gonzalez, P.L.M., Polvani, L.M., Seager, R., Correa, G.J.P., 2014. Stratospheric ozone depletion: a key driver of recent precipitation trends in south eastern South America. Clim. Dyn. 42 (7–8), 1775–1792.

Greene, A.M., Goddard, L., Cousin, R., November 2011. Web tool deconstructs variability in twentieth-century climate. EOS. Trans. Am. Geophys. Union 92 (45), 397–408, URL: http://iridl.ldeo.columbia.edu/maproom/.Global/.Time_Scales/

Greene, A.M., Hellmuth, M., Lumsden, T., 2012. Stochastic decadal climate simulations for the Berg and Breede Water Management Areas, Western Cape province, South Africa. Water Resour. Res. 48, 1–13.

Hansen, J.W., Ines, A.V.M., 2005. Stochastic disaggregation of monthly rainfall data for crop simulation studies. Agr. Forest Meteorol. 131, 233–246.

Harris, I., Jones, P.D., Osborn, T.J., Lister, D.H., 2013. Updated high-resolution grids of monthly climatic observations – the CRU TS3.10 Dataset. Int. J. Climatol. 34 (3), 623–642.
Hay, L.E., Wilby, R.L., Leavesley, G.H., 2000. A comparison of delta change and downscaled GCM scenarios for three mountainous basins in the United States. J. Am. Water. Resour. Assoc. 36 (2), 387–397.
Hegerl, G.C., Crowley, T.J., Baum, S.K., Kim, K.-Y., Hyde, W.T., 2003. Detection of volcanic, solar and greenhouse gas signals in paleo-reconstructions of Northern Hemisphere temperature. Geophys. Res. Lett. 30 (5).
Hughes, J.P., Guttorp, P., Charles, S.P., 1999. A non-homogeneous hidden Markov model for precipitation occurrence. J. R. Stat. Soc. C 48 (1), 15–30.
Ihaka, R., Gentleman, R., 1996. R: A language for data analysis and graphics. J. Comput. Graph. Stat. 5 (3), 299–314.
Jones, J.W., Hoogenboom, G., Porter, C.H., Boote, K.J., Batchelor, W.D., Hunt, L.A., Wilkens, P.W., Singh, U., Gijsman, A.J., Ritchie, J.T., 2003. The DSS cropping system model. Eur. J. Agron. 18 (3-4), 235–265.
Kang, S.M., Polvani, L.M., Fyfe, J.C., Sigmond, M., 2011. Impact of polar ozone depletion on subtropical precipitation. Science 332 (6032), 951–954.
Knutti, R., Masson, D., Gettelman, A., 2013. Climate model genealogy: Generation CMIP5 and how we got there. Geophys. Res. Lett. 40 (6), 1194–1199.
Liebmann, B., Vera, C.S., Carvalho, L.M.V., Camilloni, I.A., Hoerling, M.P., Allured, D., Barros, V.R., Báez, J., Bidegain, M., 2004. An observed trend in central South American precipitation. J. Climate 17 (22), 4357–4367.
Magrin, G.O., Travasso, M.I., Rodriguez, G.R., 2005. Changes in climate and crop production during the 20th century in Argentina. Clim. Change 72 (1-2), 229–249.
Mahalanobis, P.C., 1936. On the generalised distance in statistics. Proc. Natl. Acad. Sci. India 2 (1), 49–55.
Masson, D., Knutti, R., 2011. Spatial-scale dependence of climate model performance in the CMIP3 ensemble. J. Climate 24, 2680–2692.
Podestá, G.P., Messina, C.D., Grondona, M.O., Magrin, G.O., 1999. Associations between grain crop yields in Central-Eastern Argentina and El Niño-Southern Oscillation. J. Appl. Meteor. 38, 1488–1498.
Prairie, J., Nowak, K., Rajagopalan, B., Lall, U., Fulp, T., 2008. A stochastic nonparametric approach for streamflow generation combining observational and paleoreconstructed data. Water Resour. Res. 44 (6).
Rajagopalan, B., Lall, U., 1999. A k-nearest-neighbor simulator for daily precipitation and other weather variables. Water Resour. Res. 35 (10), 3089–3101.
Rienecker, M.M., Suarez, M.J., Gelaro, R., Todling, R., Bacmeister, J., Liu, E., Bosilovich, M.G., Schubert, S.D., Takacs, L., Kim, G.-K., Bloom, S., Chen, J., Collins, D., Conaty, A., da Silva, A., 2011. MERRA: NASA's modern-era retrospective analysis for research and applications. J. Climate 24, 3624–3648.
Schneider, U., Becker, A., Finger, P., Meyer-Christoffer, A., Rudolf, B., Ziese, M., 2011. GPCC Full Data Reanalysis Version 6.0 at 0.5°: Monthly Land-Surface Precipitation from Rain-Gauges Built on GTS-Based and Historic Data. Tech. Rep. Global Precipitation Climatology Centre (GPCC), Deutscher Wetterdienst.
Seager, R., Naik, N., Baethgen, W., Robertson, A., Kushnir, Y., Nakamura, J., Jurburg, S., 2010. Tropical oceanic causes of interannual to multidecadal precipitation variability in southeast South America over the past century. J. Climate 23 (20), 5517–5539.
Solomon, S., 1999. Stratospheric ozone depletion: A review of concepts and history. Rev. Geophys. 37 (3), 275–316.
Solomon, S., Qin, D., Manning, M., Chen, Z., Marquis, M., Averyt, K., Tignor, M., Miller, H. (Eds.), 2007. Climate Change 2007: The Physical Science Basis. Cambridge University Press, Cambridge, UK.
Son, S.-W., Tandon, N.F., Polvani, L.M., Waugh, D.W., 2009. Ozone hole and Southern Hemisphere climate change. Geophys. Res. Lett. 36 (15).
Viglizzo, E.F., Frank, F.C., 2006. Ecological interactions, feedbacks, thresholds and collapses in the argentine pampas in response to climate and farming during the last century. Quaternary Int. 158 (1), 122–126.
Wilks, D.S., Wilby, R.L., 1999. The weather generation game: a review of stochastic weather models. Prog. Phys. Geogr. 23, 329–357.